Design and Simulation of Tunneling Diodes With 2D Insulators for Rectenna Switches

Evelyn Li , Parameswari Raju , Erhai Zhao *

Posted Date: 23 January 2024

doi: 10.20944/preprints202401.1683.v1

Keywords: MIM junction; 2D insulators; Switch; tunneling diodes; rectenna; rectifying circuits

Article

Design and Simulation of Tunneling Diodes with 2D Insulators for Rectenna Switches

Evelyn Li [1], Parameswari Raju [2] and Erhai Zhao [2,*]

[1] Thomas Jefferson High School of Science and Technology, Alexandria, VA 22312, United States of America; evelynli2006et@gmail.com

[2] Department of Physics and Astronomy, George Mason University, Fairfax, VA 22030, United States of America; ezhao2@gmu.edu

* Correspondence: Prof. Erhai Zhao, ezhao2@gmu.edu;

Abstract: Rectenna is the key component in radio-frequency circuits for receiving and converting electromagnetic waves into direct current. However, it is very challenging for the conventional semiconductor diode switches to rectify high-frequency signals for 6G telecommunication (>100 GHz), medical detection (>THz) and rectenna solar cells (optical frequencies). Such a major challenge can be resolved by replacing the conventional semiconductor diodes with tunneling diodes as the rectenna switches. In this work, metal-insulator-metal (MIM) tunneling diodes based on 2D insulating materials were designed, and their performance was evaluated using a comprehensive simulation approach which includes density-function-theory simulation of 2D insulator materials, modeling of the electrical characteristics of tunneling diodes, and circuit simulation for rectifiers. It is found that novel 2D insulators such as monolayer TiO_2 can be obtained by oxidizing sulfur-metal layered materials. The MIM diodes based on such insulators exhibit fast tunneling and excellent current rectifying properties. Such tunneling diodes effectively convert the received high-frequency electromagnetic waves into direct current.

Keywords: MIM junction; 2D insulators; Switch; tunneling diodes; rectenna; rectifying circuits;

1. Introduction

In general, a typical rectenna, i.e., rectifying antenna, consists of an antenna and rectifying circuit. The rectenna was first developed by Brown in 1963 [1]. The rectifying circuit is used to convert electromagnetic (EM) waves into direct current (DC) electricity. The conventional rectifying circuits work properly with radio-frequency (RF) signals of a range from 3 kHz to 500 kHz. [2] Certain carefully-designed rectifying circuits could be operating at up to 300 MHz with bipolar junction transistors and 2 GHz with integration of multiple MOS devices [3,4]. As the telecommunication is entering into the 5G and soon 6G era, both fast response and large bandwidth are needed, pushing the limit of frequency toward the high end of RF range (>100 GHz) [5]. For example, millimeter waves (30-300 GHz) and terahertz signal will be used in 6G technology [6,7]. The 100 GHz signal demands 10 ps in response time, approaching the limit in transit time for an electron to diffuse across a silicon PN junction diode. Such a long diffusion time places a strict limit on the high-frequency application in converting alternative current (AC) into DC.

On the other hand, optical detection, as an important method for non-ionizing medical detections [8,9], has been increasingly used in wearable electronics, e.g., smart watches, to measure heartbeat, blood sugar, blood oxygen and so on. This technology requires the lights, a kind of high-frequency electromagnetic waves, to penetrate through the skin [10]. The current wearable electronics are often equipped with visible lights, e.g., green and red lights, to perform the biomedical measurement [11]. However, the medical information obtained by such wearable electronics is quite limited and not precise. THz propagation through the biological tissues would be accompanied by much less scattering loss because of its much longer wavelength compared to those of visible or

 doi:10.20944/preprints202401.1683.v1

infrared radiation [12]. It is well known that EM waves at 10^{12} Hz (THz) are able to image human tissues without harm and provide much more information at a higher resolution in comparison with other methods. For example, ultrasound, another method for non-ionizing detection, with frequencies ranging from 2 MHz to 12 MHz, has a resolution at 1 mm, much lower than that of optical and THz detection. Thus, THz electronics offer excellent safe evaluation, high resolution and precision, all of which are very attractive for future medical detections [13,14]. Since the optical and THz signal frequencies are too high for conventional semiconductor diodes, new diodes with a switching time faster than 1 ps are needed to rectify THz signal for medical detection.

In addition, rectenna has been studied for energy harvesting of 2.4 GHz EM waves for internet-of-things technology [15]. To receive and rectify EM waves at optical frequencies, e.g., solar energy, optical rectennas [16,17] become attractive high-efficiency and low-cost solar cells if fast-switching diodes can be available. The conventional solar cells are based on a semiconductor PN junction whereas electron-hole pairs are generated by photons with energy larger or close to the energy bandgap (E_g) of the semiconductors. Silicon-based solar cells in the most commercially dominated products have a limited efficiency, about 16% for polycrystalline Si, 30% for monocrystalline Si and 55% for multi-junction cells [18–20]. In comparison, the rectenna solar cells has a much higher efficiency (> 85%) and can be fabricated at low cost [16].

Therefore, the common technical challenge for the above-mentioned emerging technologies (high-speed telecommunication, THz electronics and rectenna solar cells) hinges on new rectifier diodes. As shown in Figure 1(a), in the conventional semiconductor PN junction diode, the excess carriers are injected to each side of the junction as minority carriers and diffuse through the diode. The diffusion time (τ_s) is close to the smallest value of electron lifetime (τ_e) or hole lifetime (τ_h). The lifetime of minority carrier depends on Auger lifetime due to Auger recombination [21]. In typical, for Si with a doping of 10^{18} cm^{-3}, the diffusion time is within a range from 10 ns to 1 μs, which is corresponding to switching frequencies from 1 MHz to 100 MHz. Optimization of device structures and diode materials, such as Schottky junction diodes and GaN diodes, has been studied to improve the switching frequency to GHz [22]. However, THz and optical frequencies are still too high for the conventional PN junction diodes.

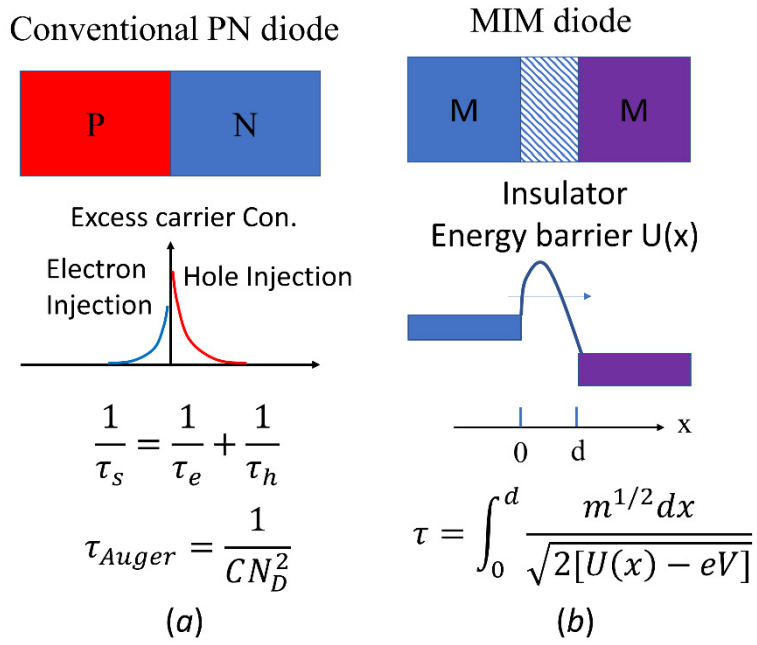

Figure 1. (a) In a conventional PN diode, the charge carriers diffuse through the depletion region. The diffusion time is usually long. (b) In a MIM tunneling junction, the electron tunnels across a thin barrier. The tunneling time is usually very short.

 doi:10.20944/preprints202401.1683.v1

On the other hand, carrier transport based on tunneling can easily exceed the limit of diffusion in PN junctions, reaching the scale of femtoseconds (10^{-15} s). The metal-insulator-metal (MIM) junction with an atomically thin insulator between two different metals is a simple yet very effective tunneling diode. A schematic of MIM tunneling diode and its energy barrier for tunneling are shown in Fig. 1(b). The electron tunneling time is determined by the energy barrier profile and applied bias across the barrier. Studies showed that the tunneling time across a tunneling diode could reach femtoseconds [23] and even attoseconds (10^{-18} s) in an atomic hydrogen. [24]

The MIM heterostructures have recently been studied as a current rectifying diode [25–28]. Research interest of MIM diodes was focused on application in rectifying high-frequency electromagnetic waves, THz electronics, infrared light and even conversion of visible light into electricity [16,29,30]. The MIM diodes based on bulk insulators, such as TiO_2, ZnO and NiO, could be applied in 28.3 THz rectenna switches [31]. Amorphous InGaZn oxide was shown to improve turn-on voltage control in the diodes [32]. Amorphous metal electrodes could also improve the current rectifying performance [33]. Recently, MIM diodes based on 2D insulator materials have been reported [34]. MIM diodes with single and multiple insulators have been studied and analyzed for the conversion of infrared light into electricity [35,36]. Despite the rapid progress, there still lacks a comprehensive study that combine first-principle calculation for designing 2D insulator materials, modeling of tunneling diodes, and simulation of rectifier circuits.

In this work, we applied density function theory (DFT) method to design and model MIM tunneling diodes with two-dimensional (2D) materials as the insulators. In the modeling, 1, 2, 3-layer TiO_2, TaO_2 and SnO_2 were designed by oxidizing the corresponding 2D metal-sulfur materials. The monolayer or few-layer 2D materials were placed between two different metals to form a tunneling junction diode. In the device simulation, it is found that the Au/monolayer TiO_2/Al tunneling junction diode exhibits the best rectifying performance. The simulated tunneling current-voltage (I-V) characteristics were fed through a rectifier in PSpice modeling, showing excellent signal rectifying from THz to optical frequencies.

2. Modeling and Simulation Method for Materials, Devices and Circuits

In this study, the atomistic simulations of 2D materials and MIM tunneling diodes were performed in QuantumWise Atomistix Toolkit (ATK) simulation platform [37–39] from Synopsys based on density functional theory (DFT). The DFT calculations employed the norm-conserving Pseudo-Dojo pseudopotentials [40] with Perdew-Burke-Ernzerhof (PBE) parametrization of exchange-correlation function [41] for all materials and diode structures. To bring all atoms to the ground state, a 12×12×1 Monkhorst-Pack k-point grid mesh was used for the sampling of the Brillouin zone. The forces were kept to the least at 0.01 eV/Å. For the calculations of carrier transport in the tunneling diodes based on metal/2D insulators/metal heterostructures, we used first-principle calculations integrated with density functional non-equilibrium Green's function (NEGF) method. In addition, the current-voltage (I-V) characteristics was calculated by following the Landauer-Büttiker approach [42]. The design of 2D materials and computation of carrier transport were implemented by using the above-mentioned QuantumWise ATK code. [37]

In the simulation of 2D materials, 1, 2, 3-layer metal-sulfur materials are designed and modeled with structural relaxation. These ultra-thin 2D metal-sulfur materials are usually semiconductors with an energy bandgap. [34] In the structural relaxation in simulation, the position of all atoms and the three-dimensional lattice parameters were optimized with the least Hellmann-Feynman force of 0.01 eV/Å on the metal-sulfur layer materials. In the optimization, Pulay-mixer algorithm was used as a fully self-consistent field (SCF) iteration control with a tolerance value of 10^{-5} eV. The maximum number of iteration steps was set at a limit of 100. The self-consistent field computations were strictly tracked to guarantee full convergence within the iteration steps. Periodic boundary conditions were employed along the three directions (in-plane and out-of-plane) with a large vacuum region of 7 Å to minimize the interlayer interaction. [43] Energy band structures and electronic properties of the metal-sulfur layer materials could be calculated once the structure optimization simulation was converged. In the design and simulation of metal-oxide layer materials, we proposed a simulated

 doi:10.20944/preprints202401.1683.v1

oxidation process: (1) the sulfur atoms were replaced with oxygen atoms; and (2) the new metal oxide materials were fully optimized by following the similar procedure in obtaining relaxed metal-sulfur layer materials.

The 2D layer oxide insulators were placed between two metal electrodes to construct metal/2D insulators/metal tunneling diodes. There is a 7-Å gap between the 2D insulators and electrodes at each side to protect the layer oxides from chemical reaction with the metal electrodes during simulation. As the layer insulators were surrounded by vacuum, our simulation was able to neglect the effect of substrate and electrodes. The simulation of tunneling current in the metal/2D insulators/metal diodes under a bias voltage was implemented by using DFT method in the Virtual Nanolab ATK package. [37] Generalized Gradient Approximation (GGA) [41] was adopted with PBE exchange correlation to describe and include the electron correlation and exchange energies in the calculation of carrier transport under bias voltage.

The design and modeling of a full-bridge AC/DC power converter built on the proposed MIM diodes was done in OrCAD PSpice simulation tool. [44] In the circuit simulation, a PSpice device model was built for the MIM tunneling diodes by implementing the I-V characteristics and tunneling time obtained in above-mentioned DFT calculations. An AC voltage input of 1.0 V at 100 kHz was applied in the simulation and a DC output was analyzed to evaluate the performance of proposed MIM tunneling diodes. The output voltage as a function of the frequency of received signals from 1 Hz to 1000 THz was simulated based on the calculated tunneling time to analyze the high-frequency performance.

3. Results and Discussion

3.1. Molecular structures and Energy Bands of 2D metal oxide insulators

Figure 2(a) shows the design of MIM tunneling diodes with the 2D insulator material sandwiched between the top and bottom metal electrodes. The two electrodes have a different work function, enabling current rectifying functionality of the MIM diodes. The key element of the diodes is the middle 2D insulator and its interface with metal electrodes. It is desirable to use insulators with a low tunneling barrier height, i.e., high electron affinity, such as TiO_2, SnO_2 and Ta_2O_5, for low-voltage current rectifying [33,34]. Lower barrier height generally leads to higher tunneling rate. However, the efficiency of tunneling current also depends on the quality of the interface between insulator and metal electrodes. The proposed 2D insulators have a smooth and self-passivated surface, very favorable for tunneling. As shown in Figure 2(b), the 2D layer-structured oxide insulators, such as TiO_2, SnO_2 and TaO_2, can be obtained by oxidizing the counter parts 2D metal sulfur layer materials, such as TiS_2, SnS_2 and TaS_2. These 2D layer materials are van de Waals materials with monolayer or multilayer, whereas the S atoms can be replaced with O atoms by oxidation. In the simulation, the oxidation is expressed by replacement of S atoms with O atoms followed by a structural relaxation to achieve stable 2D oxide layer materials.

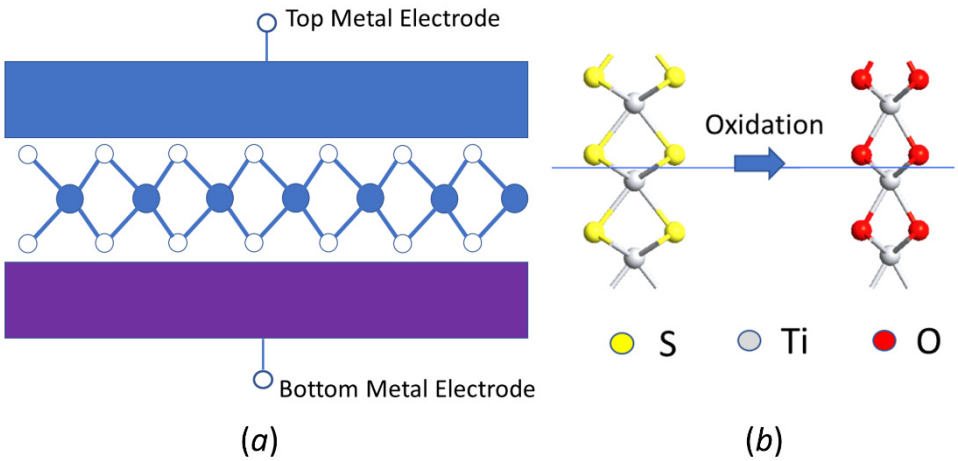

 doi:10.20944/preprints202401.1683.v1

Figure 2. (a) Schematic of MIM junction with 2D layered insulators being sandwiched by top and bottom electrodes. (b) Possible 2D metal oxide insulators can be obtained by oxidizing metal sulfides.

Figure 3 shows the energy band structures of hexagonal TiS_2 and TiO_2 obtained from the DFT simulation. As mentioned above, the 2D TiO_2 materials are achieved by replacing S atoms in TiS_2 with O atoms followed by a structural relaxation and optimization. The DFT calculation of 2D oxides converged at a minimal force of 0.01 eV/Å, achieving a stable layer structure which can be obtained in experiment and production. After such a proper structural relaxation, energy band structures and electronic properties of each monolayer, bilayer and trilayer structures can be reasonable evaluated.

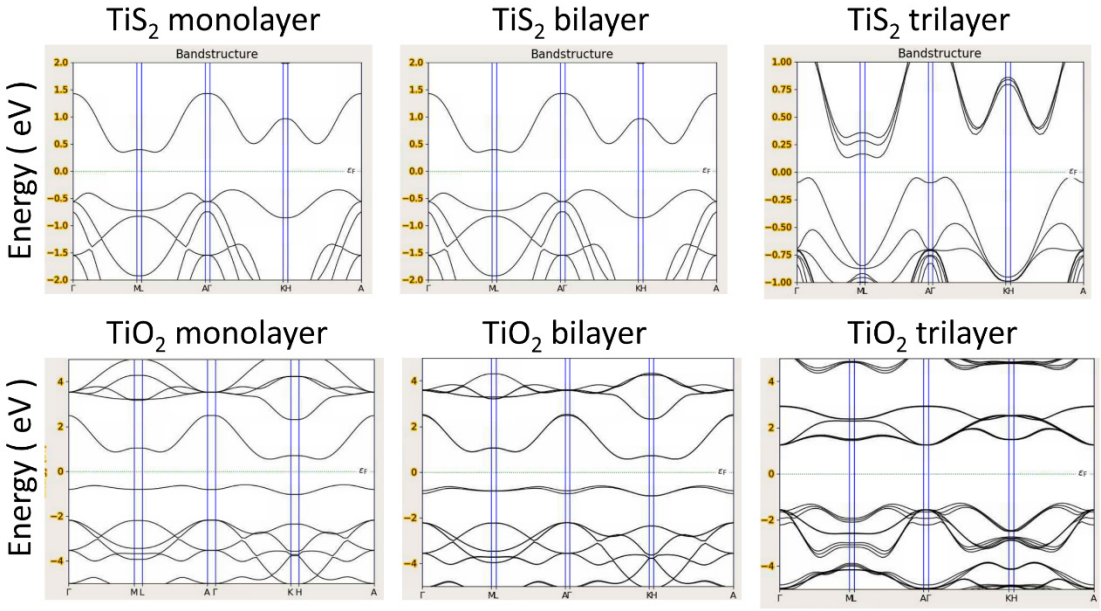

Figure 3. Energy band structures of monolayer, bilayer and trilayer TiS_2 and TiO_2.

The result indicates that the 1, 2, 3-layer TiO_2 materials have a significant bandgap and can be considered as insulators. The energy bandgap value increases from 1.8 eV for monolayer TiO_2 to 3.1 eV for trilayer TiO_2. The 2D TiO_2 have a significantly larger bandgap than the counterparts of 2D TiS_2. TiS_2 is considered as a semiconductor with a relatively small energy bandgap. [45-46] The simulated band gap for monolayer materials is lower than that of bulk materials because the spin-orbit coupling (SOC) was not considered in calculation [47, 48]. Nonetheless, the materials structure and electrical properties of 2D TiO_2 are successfully modeled and can be used for the simulation of carrier transport, tunneling diodes and voltage conversion circuits.

Similar DFT simulation processes are also performed on the TaS_2 and SnS_2 layer materials, and the TaO_2 and SnO_2 layer materials obtained via oxidation of the metal-sulfur counterparts. Figure 4 shows the molecular structures of the above-mentioned trilayer Materials. The 2D layer materials were designed with thin vacuum region (7 Å) surrounding them to minimize chemical interaction with substrate or electrodes. These 2D TaS_2, SnS_2, TaO_2 and SnO_2 were then optimized with structural relaxation using QuantumWise ATK code. [37,41] The energy band structures of TaS_2 and TaO_2 mono-, bi-, and trilayer are shown in Figure 5. The result indicates that a significant band gap exists in TaO_2 layered materials while the band gap is negligible in TaS_2 layered materials, which has been previously reported [49]. Also, the band gap of 2D TaO_2 (about 0.7 eV) does not change appreciably with increasing number of layers, which is different with that of TiO_2. In addition, the band structures of 2D TaO_2 materials look like the ones of n-type semiconductors with Fermi level merged into the conduction band.

Preprints.org (www.preprints.org) | NOT PEER-REVIEWED | Posted: 23 January 2024 doi:10.20944/preprints202401.1683.v1

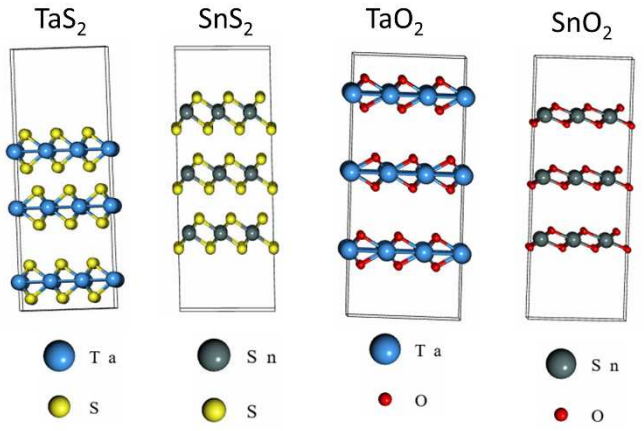

Figure 4. Design of molecular structures for trilayer TaS_2, SnS_2, TaO_2 and SnO_2 in simulation.

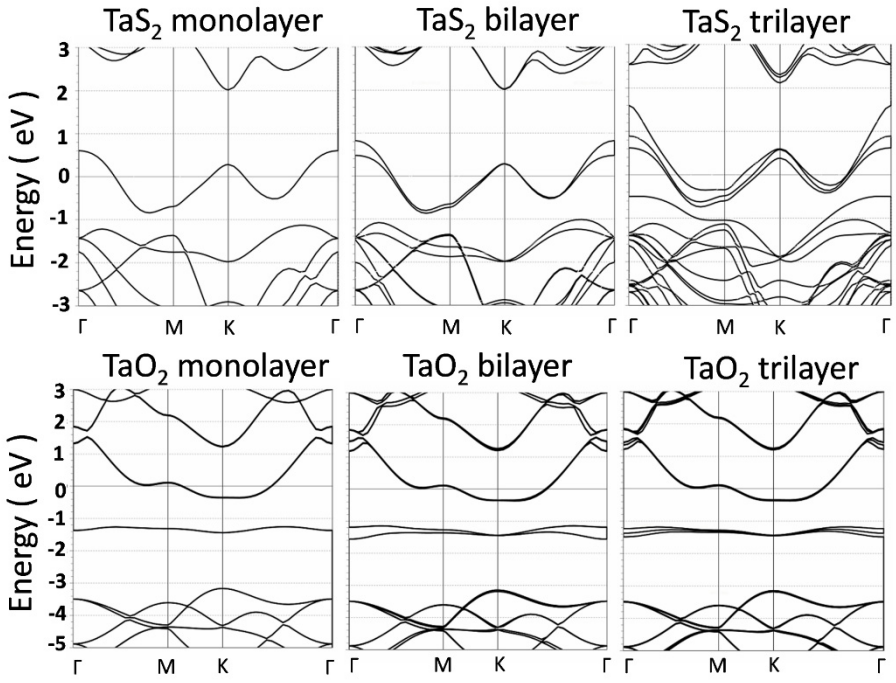

Figure 5. Energy band structures of TaS_2 and TaO_2 monolayer, bilayer and trilayer.

Figure 6 shows the energy band structures of mono-, bi- and trilayer SnS_2 and SnO_2 materials. The 2D SnS_2 layer materials have a significant indirect bandgap about 1.6 eV.

 doi:10.20944/preprints202401.1683.v1

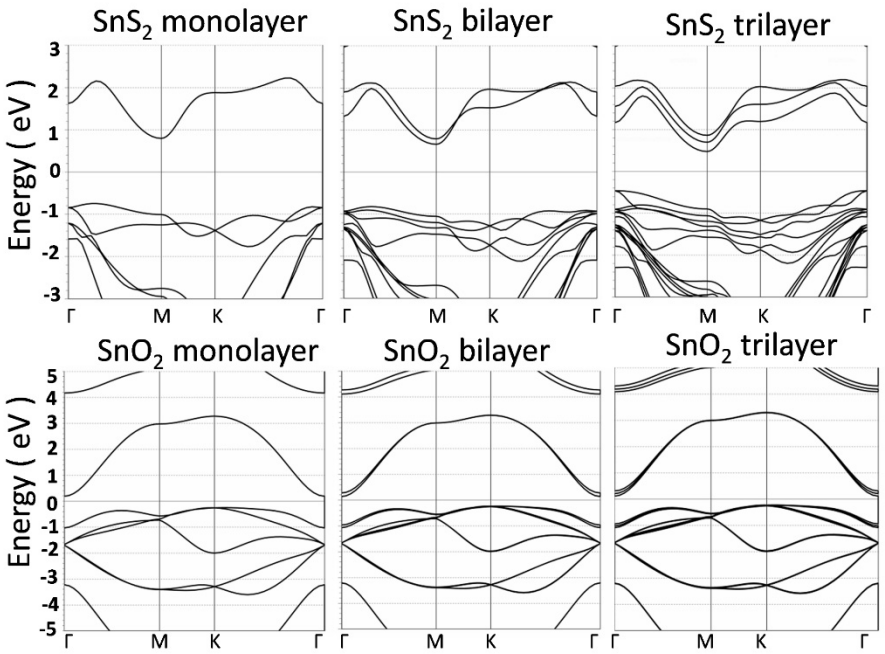

Figure 6. Energy band structures of SnS_2 and SnO_2 monolayer, bilayer and trilayer.

However, the energy band gap of SnO_2 layered materials disappears after the SnS_2 is oxidized with the S atoms being replaced by O atoms. From the observation from the band structures, the SnO_2 layer materials look more like a semimetal with zero bandgap than a semiconductor or insulator. The result indicates that the SnO_2 layer materials are not a good choice as 2D insulators for application in the proposed MIM diodes.

3.2. Design and electrical properties of MIM diodes with 2D insulators

As seen from the DFT calculations, although some 2D metal oxide materials are not a good choice for insulators, excellent 2D materials can be screened and found by using such a simulating oxidation experiment based on DFT calculation. The next step is to design a MIM diode using the modeled 2D insulators and study its electrical properties. As shown in Figure 7, MIM diodes are constructed with monolayer, bilayer or trilayer TiO_2 being sandwiched between Au and Al electrodes. The 2D TiO_2 films act as the smooth, ultra-thin tunneling barrier for electron to transport between two metal electrodes. In the design of Au/TiO_2/Al heterojunction, 9 atomic layers of Au and Al have been employed to maintain the structure of metal during the structural relaxation in the simulation. This significantly increases the computation time in the simulation since a large number of atoms are included. However, this design is sufficiently close to the real devices in which metal films are much thicker than 2D insulators and will not experience structural change due to lattice difference with the 2D materials. It should be noted that the metal structures have an unreal change in structural relaxation if only < 5 atomic layers of metals are used in simulation whereas the thickness of metal is comparable to the inserted 2D insulators. In addition, the design of MIM tunneling diodes is not limited to 2D TiO_2 and can be applied to other 2D insulators.

Preprints.org (www.preprints.org) | NOT PEER-REVIEWED | Posted: 23 January 2024 doi:10.20944/preprints202401.1683.v1

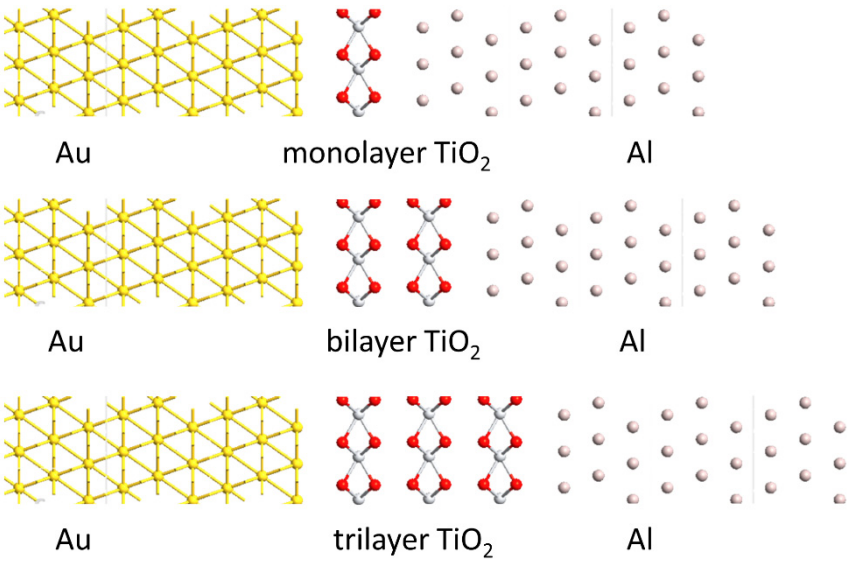

Figure 7. Design of Au/TiO2/Al MIM tunneling diodes with monolayer, bilayer and trilayer TiO2.

Figure 8 shows the I-V characteristics of Au/TiO2/Al tunneling diodes with monolayer, bilayer and trilayer of TiO2 at room temperature. In the simulation, an electric bias voltage from -1.0 V to 1.0 V is applied on MIM diodes at a step of 0.2V. The I-V curves exhibit a junction-like current rectifying function with low resistance for current flowing from Au electrode to Al electrode and high resistance along the opposite direction. Although all three MIM diodes have current rectifying capability, the current density decreases exponentially with increasing layer numbers of TiO2 films. In addition, the I-V curves become less exponential, i.e., current on/off ratio within a certain voltage window decreases, as the number of TiO2 layer increases. This indicates that the rectifying capability decreases with increasing thickness of TiO2 layer materials. Our study shows that the Au/monolayer TiO2/Al diode exhibits the best current rectifying characteristics. In the circuit modeling (to be discussed later), we selected the Au/monolayer TiO2/Al tunneling diode as the switching diode model for voltage conversion and adjusted the current level or diode resistance for application by choosing the right cross-section area. It should be noted that the tunneling time is not be affected by the device area.

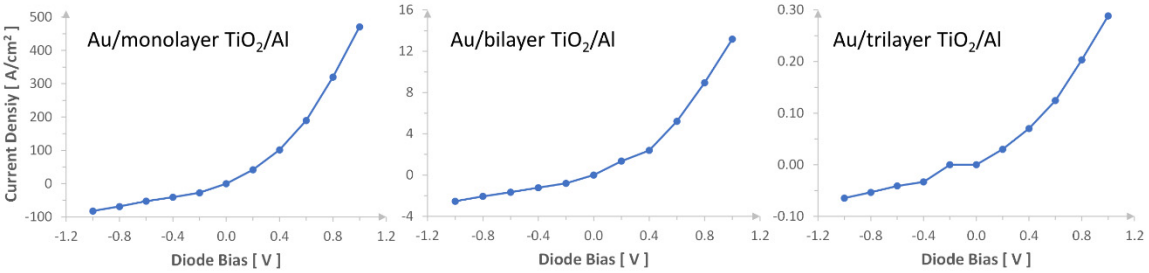

Figure 8. The current-voltage (IV) characteristics for Au/TiO2/Al tunneling diodes.

The tunneling time is an important parameter for rectifier diodes. It directly determines the upper limit of switching frequency that the rectifier can handle. In this work, the tunneling time of the Au/monolayer TiO2/Al diode have been studied and calculated for different bias voltages. Figure 9 shows the electron affinity extracted from the simulation for the monolayer TiO2 between Au and Al electrodes. A trapezoid shape of tunneling barrier is drawn along the extract value of electron affinity for each bias voltage (see Figure 9(a)-(c)). The trapezoid barrier profile will be used for the

 doi:10.20944/preprints202401.1683.v1

calculation of tunneling time. The tunneling time can be calculated using the integration equation shown in Figure 1(b) following the method by Buttiker and Sinton [50,51]. As shown in Figure 9(d), the tunneling time decreases slightly from 1.85 fs to 1.65 fs with increasing bias from 0 V to 1.0 V. Such a short switching time enables the proposed diode to effectively rectify high-frequency signal up to 600 THz. It should be noted that the simulation does not consider the impact of impurity and defect at the interface and inside the 2D materials. The interface impurity and defect usually increase tunneling time and decrease tunneling current, which should be an important issue to examine in experiment. Nonetheless, the proposed metal/2D insulator/metal tunneling diodes exhibit excellent current rectifying capability with an ultra-fast switching time reaching femtosecond (10^{-15} s).

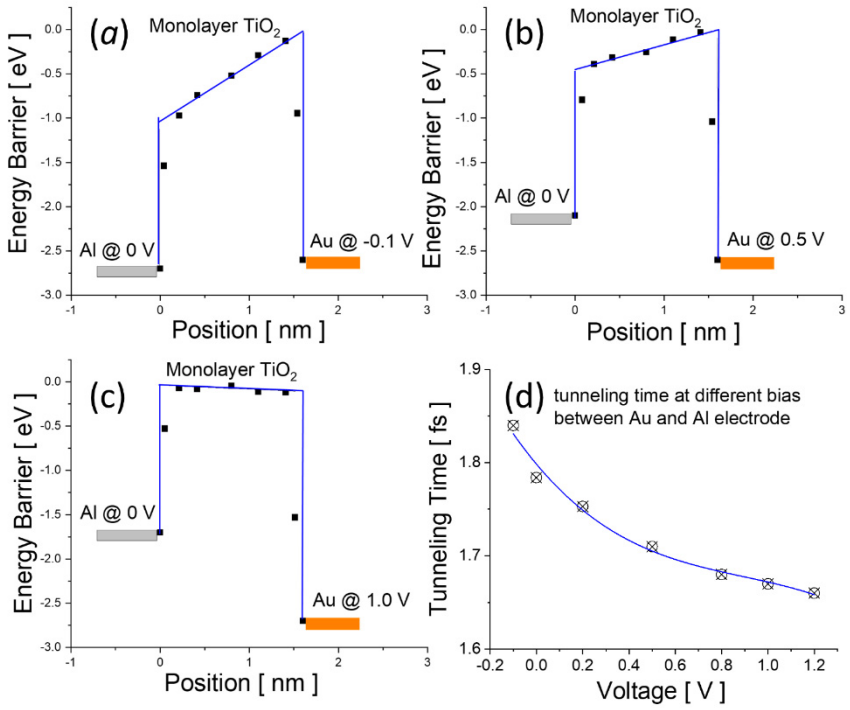

Figure 9. Electron affinity profile of monolayer TiO_2 at position along current flowing direction is extracted when the diode is biased at (a) -0.1V, (b) 0.5V and (c) 1.0V. A trapezoid marked in blue is drawn along the electron affinity to represent the tunneling barrier for each case. (d) Tunneling time for each bias is calculated according the method described in Figure 1.

3.3. Circuit simulation of rectifiers based on 2D MIM tunneling diodes

The performance of 2D MIM tunneling diodes can be full evaluated in a rectifying circuit. Figure 10(a) shows a schematic of rectenna circuit with both an antenna and a full-wave bridge rectifying circuit. In the rectifier circuit, D1, D2, D3 and D4 are identical diodes based on the above-simulated Au/monolayer TiO_2/Al MIM tunneling diode with the I-V characteristics shown in Figure 8 and tunneling time (1.6 fs) derived in Figure 9(d). The diodes have a cross-section area of 10^{-4} cm^2 (i.e., 100 μm × 100 μm), exhibiting an on-state current at the range of 10 mA to 40 mA. The circuit simulation was carried out and analyzed in OrCAD PSpice Integrated Simulation platform [44]. In the circuit design, the antenna is replaced with an AC voltage source which is tunable in voltage and frequency. Both the AC-to-DC conversion and high-frequency performance were studied and analyzed. Figure 10(b) shows that the rectifying circuit effectively converts a 1.0-V, 100kHz AC input, simulated signal received by antenna, into a 0.7-V DC voltage output. The DC output voltage is stabilized within 20 ms, exhibiting a robust AC/DC conversion with the proposed 2D MIM tunneling diodes. Figure 10(c) shows the DC output voltage as a function of frequency of input AC signals in circuit simulation. The rectifying circuit based on the proposed monolayer TiO_2 MIM tunneling diode successfully maintained a DC output voltage of about 0.7 V for up to 800 THz, agreeing with the switching time

 doi:10.20944/preprints202401.1683.v1

of the tunneling diodes. Such a frequency range is very attractive for medical detection, rectenna solar cell and high-speed telecommunication.

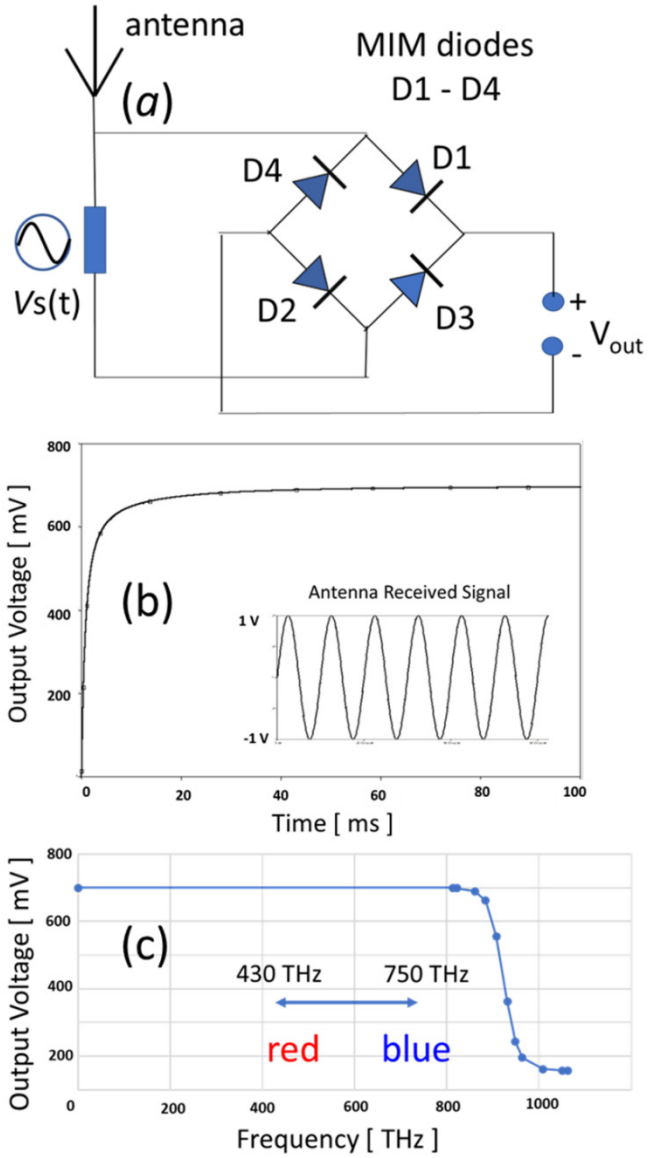

Figure 10. (a) Schematic of a rectenna circuit with a full-wave bridge rectifier based on the modeled monolayer TiO_2 MIM diode. (b) Simulation of the rectifier which converts AC signal to DC output. (c) DC output voltage as a function of input AC frequency. The rectifier maintains a constant DC output at 0.7 V for up to 800 THz.

4. Conclusions

In summary, we have designed, simulated and investigated a family of 2D insulators by oxidizing metal sulfides by using DFT method. The I-V characteristics of metal/insulator/metal junctions with the chosen 2D insulators exhibit excellent rectifying capability with a significant dependence on the number of layers. The diode tunneling time has also been studied, showing promising potential for THz electronics. In addition, we have successfully designed and simulated an AC-to-DC rectifying circuit based on the proposed monolayer TiO_2 MIM tunneling diode. The rectifier is able to robustly convert AC voltage input into DC voltage output. The rectifier circuit is well functional at high frequency up to 800 THz. Such rectifying switches based on the proposed 2D insulator MIM tunneling diodes are very attractive in many applications including medical detection, 5G/6G telecommunication and rectenna solar cells.

Author Contributions: Conceptualization, E.L. and E.Z.; methodology, E.L. and E.Z.; software, E.L. and P.R.; validation, E.L P.R. and E.Z..; formal analysis, E.L.; investigation, E.L.; resources, E.Z.; data curation, E.L.; writing—original draft preparation, E.L.; writing—review and editing, E.Z.; visualization, E.L. and P.R.; supervision, E.Z.; project administration, E.Z.; funding acquisition, E.Z. All authors have read and agreed to the published version of the manuscript.

Funding: Please add: Authors are grateful to the support of George Mason University and Thomas Jefferson High School of Science and Technology on computing resource.

Institutional Review Board Statement: Not applicable.

Data Availability Statement: Data available on request.

Acknowledgments:

We gratefully acknowledge support by the Office of Research Computing at George Mason University (URL: https://orc.gmu.edu).

Conflicts of Interest: The authors declare no conflicts of interest.

References

1. Brown, W.; George, R.; Heenan, N.; Wonson, R.; Microwave to DC converter. US patent: US3434678A, 1969.
2. Basak, M.; Kacar, F. Realization of current-mode fully integrated full-wave rectifier. AEU - International Journal of Electronics and Communications 2017, 82, 45.
3. Kumngern, M.; Dejhan, K. A New Translinear-Based Dual-Output Square-Rooting Circuit. Active and Passive Electronic Components 2008, 6, 623970
4. Xu, Z.; Khalifa, A.; Mittal, A.; Nasrollahpourmotlaghzanjani, M.; Etienne-Cummings, R.; Sun, N.; Cash, S.; Shrivastava, A. Analysis and Design Methodology of RF Energy Harvesting Rectifier Circuit for Ultra-Low Power Applications. IEEE Open J. Circuits and Systems 2022, 3, 82.
5. Rappaport, T.; Xing, Y.; Kanhere, O.; Ju, S.; Madanayake, A.; Mandal, S.; Alkhateeb, A.; Trichopoulos, Georgios C. Wireless Communications and Applications Above 100 GHz: Opportunities and Challenges for 6G and Beyond. IEEE Access 2019, 7, 78729.
6. Jiang, W.; Zhang, Q.; He, J.; Habibi, M.A.; Melnyk, S.; El-Absi, M.; Han, B.; Renzo, M.D.; Schotten, H.D.; LUO, F.L.; et al. Terahertz Communications and Sensing for 6G and Beyond: A Comprehensive View. arXiv 2023, arXiv:2307.10321.
7. Zinchenko, I.I.; Lapinov, A.V.; Vdovin, V.F.; Zemlyanukha, P.M.; Khabarova, T.A. Measurements and Evaluations of the Atmospheric Transparency at Short Millimeter Wavelengths at Candidate Sites for Millimeter- and Sub-Millimeter-Wave Telescopes. Appl. Sci. 2023, 13, 11706.
8. Kazanskiy, N.L.; Khonina, S.N.; Butt, M.A.; Kaźmierczak, A.; Piramidowicz, R. State-of-the-Art Optical Devices for Biomedical Sensing Applications—A Review. Electronics 2021, 10, 973.
9. Ochoa M.; Algorri J.; Roldán-Varona P.; Rodríguez-Cobo L.; López-Higuera J. Recent Advances in Biomedical Photonic Sensors: A Focus on Optical-Fibre-Based Sensing. Sensors 2021, 21, 6469.
10. Wu, W.; Wang, L.; Yang, Y.; Du, W.; Ji, W.; Fang, Z.; Hou, X.; Wu, Q.; Zhang, C.; Li, L. Optical flexible biosensors: From detection principles to biomedical applications. Biosensors and Bioelectronics 2022, 210, 114328.
11. Vavrinsky, E.; Esfahani, N.E.; Hausner, M.; Kuzma, A.; Rezo, V.; Donoval, M.; Kosnacova, H. The Current State of Optical Sensors in Medical Wearables. Biosensors 2022, *12*, 217.
12. Pirzada, M.; Altintas, Z. Recent Progress in Optical Sensors for Biomedical Diagnostics. Micromachines 2020, 11, 356.
13. Aghasi, H.; Naghavi, S.; Tavakoli Taba, M.; Aseeri, M.; Cathelin, A.; Afshari E. Terahertz electronics: Application of wave propagation and nonlinear processes. Appl. Phys. Rev. 2020, 7, 021302.
14. Gong, A.; Qiu, Y.; Chen, X.; Zhao, Z.; Xia L.; Shao Y. Biomedical applications of terahertz technology, Applied Spectroscopy Reviews 2020, 55, 418.
15. Shafique, K.; Khawaja, B.; Khurram, M.; Sibtain, S.; Siddiqui, Y.; Mustaqim, M.; Chattha, H.; Yang, X. Energy Harvesting Using a Low-Cost Rectenna for Internet of Things (IoT) Applications. IEEE Access 2018, 6, 30932.
16. Moddel, G.; Grover, S. (eds) Rectenna Solar Cells. Springer, New York, NY. 2013, DOI 10.1007/978-1-4614-3716-1
17. Sanchez A.; Davis C.; Liu K.; Javan A. The MOM tunneling diode: theoretical estimate of its performance at microwave and infrared frequencies. J Appl Phys. 1978, 49, 5270.
18. Shockley, W.; Quiesser, H.J. Detailed balance limit of efficiency of p-n junction solar cells. J. Appl. Phys. 1961, 32, 510.

19. Henry, C.H. Limiting efficiencies of ideal single and multiple energy gap terrestrial solar cells. J. Appl. Phys. 1980, 51, 4494.
20. Donchev, E.; Pang, J.; Gammon, P.; Centeno, A.; Xie, F.; Petrov, P.; Breeze, J.; Ryan, M.;Riley, D.; Alford, N. The rectenna device: From theory to practice (a review). MRS Energy & Sustainability 2014, 1, E1.
21. Sze, S.; Ng, K. Physics of Semiconductor Devices. John Wiley & Sons 2006, pp. 77-133.
22. Sun, R.; Lai, J.; Chen, W.; Zhang, B. GaN Power Integration for High Frequency and High Efficiency Power Applications: A Review. IEEE Access 2020, 8, 15529,
23. Saiadh, U. S.; Xu, H.; Wang, X.; Atia-Tul-Noor, A.; Wallace, W.; Douguet, N.; Bray, A.; Ivanov, I.; Bartschat, K.; Kheifets, A.; Sang, R. T.; Litvinyuk, I. Attosecond angular streaking and tunnelling time in atomic hydrogen. Nature 2019, 568, 75.
24. Teki, S.; Weerakkody, A.; Sedghi, N.; Hall, S.; Werner, M.; Wrech, J.; Chalker, P.; Mitrovic, I. Single and triple insulator Metal-Insulator-Metal diodes for infrared rectennas. Solid-State Electronics 2021, 185, 108096.
25. Berland B. National Renewable Energy Laboratory Final Report. 2003, see: http://www.nrel.gov/docs/fy03osti/33263.pdf.
26. Hobbs, P.; Laibowitz, R.; Libsch, F. Ni–NiO–Ni tunnel junctions for terahertz and infrared detection. Applied Optics 2005, 44, 6813.
27. Krishnan, S.; Stefanakos, E.; Bhansali, S. Effects of dielectric thickness and contact area on current–voltage characteristics of thin film metal–insulator–metal diodes. Thin Solid Films 2008, 516, 2244.
28. Bean, J.; Tiwari, B.; Bernstein, G.; Fay, P.; Porod, W. Thermal infrared detection using dipole antenna-coupled metal-oxide-metal diodes. J. Vac. Sci. Technol. B 2009, 27, 11.
29. Jin, J.; Wang, L.; Zheng, Z.; Zhang, J.; Hu, X.; Lu, J.; Etor, D.; Pearson, C.; Song, A.; Wood, D.; Gallant, A.; Balocco, C. Metal-insulator-metal diodes based on alkyltrichlorosilane self-assembled monolayers. AIP Advances 2019, 9, 065017.
30. Chen, P.; Salas, R.; Farhat, M. Generation of high-power terahertz radiation by nonlinear photon-assisted tunneling transport in plasmonic metamaterials. J. Opt. 2017, 19, 124012.
31. Tekin, S.; Almalki, S.; Finch, H.; Vezzoli, A.; O'Brien, L.; Dhanak, V.; Hall, S.; Mitrovic, I. Electron affinity of metal oxide thin films of TiO2, ZnO, and NiO and their applicability in 28.3 THz rectenna devices. Journal of Applied Physics 2023, 134, 8.
32. Kim, K.; Park, J.; Lee, D.; Cho, Y.; Kim, Y. Precise Turn-On Voltage Control of MIOSM Thin-Film Diodes with Amorphous Indium–Gallium–Zinc Oxide. ACS Applied Materials & Interfaces 2021, 13, 878.
33. Cowell, E.; Alimardani, N.; Knutson, C.; Conley, J.; Keszler, D.; Gibbons, B.; Wager, J. Advancing MIM Electronics: Amorphous Metal Electrodes. Adv. Mater., 2011, 23, 74.
34. Cui, Q.; Sakhdari, M.; Chamlagain, B.; Chuang, H.; Liu, Y.; Cheng, M.; Zhou, Z.; Chen, P. Ultrathin and Atomically Flat Transition-Metal Oxide: Promising Building Blocks for Metal–Insulator Electronics. ACS Applied Materials & Interfaces 2016, 8, 34552.
35. Belkadi, A.; Weerakkody, A.; Moddel, G. Demonstration of resonant tunneling effects in metal-double-insulator-metal (MI2M) diodes. Nature Communication 2021, 12, 2925.
36. Matsuura, D.; Shimizu, M.; Yugami, H. High-current density and high-asymmetry MIIM diode based on oxygen-non-stoichiometry controlled homointerface structure for optical rectenna. Sci. Rep. 2019, 9, 19639.
37. Smidstrup, S.; Stradi, D.; Wellendorff, J.; Khomyakov, P.; Vej-Hansen, U.; Lee, M.; Ghosh, T.; Jónsson, E.; Jónsson, H.; Stokbro, K. First-principles Green's-function method for surface calculations: A pseudopotential localized basis set approach. Phys. Rev. B 2017, 96, 195309.
38. Smidstrup, S.; Markussen, T.; Vancraeyveld, P.; Wellendorff, J.; Schneider, J.; Gunst, T.; Verstichel, B.; Stradi, D.; Khomyakov, P.A.; Vej-Hansen, U.G.; Lee, M.; Chill, S.; Rasmussen, F.; Penazzi, G.; Corsetti, F.; Ojanperä, A.; Jensen, K.; Palsgaard, M.; Martinez, U.; Blom, A.; Brandbyge, M.; Stokbro K. QuantumATK: An Integrated Platform of Electronic and Atomic-Scale Modelling Tools. J. Phys. Condens. Matter 2020, 32, 015901.
39. Yu, S.; Zhu, H.; Eshun, K.; Arab, A.; Badwan, A.; Li, Q. A computational study of the electronic properties of one-dimensional armchair phosphorene nanotubes. J. Appl. Phys. 2015, 118, 164306.
40. Van Setten, M.J.; Giantomassi, M.; Bousquet, E.; Verstraete, M.J.; Hamann, D.R.; Gonze, X.; Rignanese, G.M. The PseudoDojo: Training and grading a 85 element optimized norm-conserving pseudopotential table. Comput. Phys. Commun. 2018, 226, 39–54.
41. Perdew, J.P.; Burke, K.; Ernzerhof, M. Generalized gradient approximation made simple. Phys. Rev. Lett. 1996, 77, 3865.
42. Büttiker, M.; Imry, Y.; Landauer, R.; Pinhas, S. Generalized many-channel conductance formula with application to small rings. Phys. Rev. B 1985, 31, 6207.
43. Makov, G.; Payne, M. C. Periodic boundary conditions in ab initio calculations. Phys. Rev. B 1995, 51, 4014.
44. OrCAD Pspice Circuit Simulation Tool, https://www.orcad.com/pspice
45. Logothetis, E.M.; Kaiser, W.J.; Kukkonen, Carl A.; Faile, S.P.; Colella, R.; Gambold, J. Transport properties and the semiconducting nature of TiS2. Physica B+C 1980, 193.

 doi:10.20944/preprints202401.1683.v1

46. Wang, H.; Qiu, Z.; Xia, W.; Ming, C.; Han, Y.; Cao, L.; Lu, J.; Zhang, P.; Zhang, S.; Xu, H.; and Sun, Y. Semimetal or Semiconductor: The Nature of High Intrinsic Electrical Conductivity in TiS_2. J. Phys. Chem. Lett. 2019, 10, 6996.
47. Yu, S.; Rice, Q.; Tabibi, B.; Li, Q.; Seo, F.J. Piezoelectricity in WSe2/MoS2 heterostructure atomic layers. Nanoscale 2018, 10, 12472.
48. Yu, S.; Shi, W.; Li, Q.; Xu, F.; Gu, L.; Wang, X. Reconfigurable spin tunnel diodes by doping engineering VS2 monolayers. Phys. Chem. Chem. Phys. 2023, 25, 26211.
49. Ricci, M.; Ambrosetti, A.; Silvestrelli, P. L. Improving the Description of Interlayer Bonding in TiS2 by Density Functional Theory. J. Phys. Chem. C 2020, 124, 27592.
50. Buttiker M.; Landauer, R. Traversal Time for Tunneling. Phys. Rev. Lett. 1982, 49, 1739.
51. Sinton R. A.; Swanson, R. M. Recombination in highly injected silicon. IEEE Transactions on Electron Devices 1987, 34, 1380.